2-10-2016

# High contrast ultrasonic imaging of resin-rich regions in graphite/epoxy composites using entropy

Michael S. Hughes

John E. McCarthy
*Washington University in St Louis*, mccarthy@wustl.edu

Paul J. Bruillard

Jon N. Marsh

Samuel A. Wickline

# High contrast ultrasonic imaging of resin-rich regions in graphite/epoxy composites using entropy

Michael S. Hughes, John E. McCarthy, Paul. J. Bruillard, Jon N. Marsh, and Samuel A. Wickline

Citation: AIP Conference Proceedings **1706**, 120002 (2016); doi: 10.1063/1.4940587
View online: http://dx.doi.org/10.1063/1.4940587
View Table of Contents: http://scitation.aip.org/content/aip/proceeding/aipcp/1706?ver=pdfcov
Published by the AIP Publishing

# High Contrast Ultrasonic Imaging of Resin-Rich Regions in Graphite/Epoxy Composites Using Entropy

Michael S. Hughes[1,a)], John E. McCarthy[2], Paul. J. Bruillard[1], Jon N. Marsh[3] and Samuel A. Wickline[3]

[1]*Pacific Northwest National Laboratory, Richland, WA 99354, USA*
[2]*Depart of Mathematics, Washington University in St. Louis, St Louis, MO, USA*
[3]*Washington University School of Medicine, St Louis, MO, USA*

[a)]Corresponding author: michael.s.hughes@pnnl.gov

**Abstract** This study compares different approaches for imaging a near-surface resin-rich defect in a thin graphite/epoxy plate using backscattered ultrasound. The specimen was created by cutting a circular hole in the second ply; this region filled with excess resin from the graphite/epoxy sheets during the curing process. Backscattered waveforms were acquired using a 4 in. focal length, 5MHz center frequency broadband transducer, scanned on a 100x100 grid of points that were 0.03x0.03 in. apart. The specimen was scanned with the defect side closest to the transducer. Consequently, the reflection from the resin-rich region cannot be gated from the large front-wall echo. At each point in the grid 256 waveforms were averaged together and subsequently used to produce peak-to-peak, Signal Energy (sum of squared digitized waveform values), as well as entropy images of two different types (a Renyi entropy , and a joint entropy ). As the figure shows, all of the entropy images exhibit better border delineation and defect contrast than the either the peak-to-peak or Signal Energy. The best results are obtained using the joint entropy of the backscattered waveforms with a reference function. Two different references are examined. The first is a reflection of the insonifying pulse from a stainless steel reflector. The second is an approximate optimum obtained from an iterative parametric search. The joint entropy images produced using this reference exhibit three times the contrast obtained in previous studies.

## INTRODUCTION

In an earlier manuscript we reported on the application of thermodynamic quantities as signal receivers, *i.e.*, mathematical operations that reduce a waveform to a single number, for the study of foreign objects embedded in graphite/epoxy composites[1]. One of these was the continuous entropy (referred to as $H_C$ in that manuscript but in later publications denoted by $H_f$ to stress its dependence on the backscattered waveform $f(t)$), the others were specific heat, Topological entropy, partition function, and Thermodynamic energy which were used to define the pixel values in images of the specimen. While waveform analysis based on these yielded images of the defects that had clearer border delineation and defect region contrast, their interpretation for signal processing remained obscure. Subsequently, we have investigated new analysis techniques based on extensions of the continuous entropy, which we report here. All are different types of entropies: Renyi entropy ($I(r)$)[2], a limiting form of this entropy ($I_{f,\infty}$)[3], and joint entropy ($H_{f,g}$)[4]. One of the advantages of these quantities over the thermodynamic quantities is their extensive history in signal analysis. In addition, $H_{f,g}$ analysis triples the best previous value for defect contrast (published in [1]).

Many studies have demonstrated the utility of these different entropies for detection of subresolution backscattering structures in both materials characterization and medical ultrasonics in situations where other approaches fail. These include detection of unresolvable near-surface defects[5, 6, 7, 8, 9, 4], diffuse accumulation of subresolution-sized nanoparticle-based ultrasound contrast agents[1, 10, 11, 12, 13], characterization of smooth muscle pathologies[14, 15], and monitoring of ultrasonically induced temperature rise in tissue.[16]

*42nd Annual Review of Progress in Quantitative Nondestructive Evaluation*
AIP Conf. Proc. 1706, 120002-1–120002-7; doi: 10.1063/1.4940587

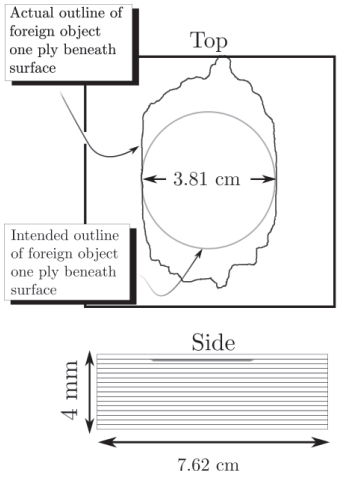


**FIGURE 1.** Drawing of the graphite/epoxy composite imaged for this study. The intended defect shape was circular. However, the curing process resulted in a different defect shape as shown. This shape was verified by destructive examination of the sample after data acquisition.

We have recently applied these newer entropies to extend previous results[17] on the detection of foreign objects. In this note we focus on improvements in the detection of resin-rich regions, which is the most difficult to detect case.

## DATA ACQUISITION

Since this study focuses on a subset of data from a much larger study which was previously published[9] we briefly summarize the acquisition of data used for this study. The basic morphology of the specimen is shown in Fig. (1).

The specimen was created by cutting a circular hole in the second ply; this region filled with excess resin from the graphite/epoxy sheets during the curing process. The presence of these foreign objects can critically degrade material strength; therefore their detection is of interest to the manufacturer. During the curing process excess epoxy seeped out of the circular region creating the elongated defect shown indicated in the figure. This was detected by several of the entropy images and was independently verified by destructive analysis of the specimen.

The specimen was scanned using a 1 in. diameter, 5 MHz center frequency (with a 3 dB bandwidth of 4.30 MHz), 4 in. focal length transducer. The transducer-to-specimen distance was 4 in., *i.e.*, the transducer was focused on the specimen surface. A computer controlled apparatus comprised of an x-y-z motion controller (to which the transducer was mounted during data acquisition), a digitizer (LeCroy 9400A), and an ultrasonic pulser/receiver (Panametrics 5800) was used to acquire data on a 100x100 grid of points that were 0.03 in. ×0.03 in. apart and covered a 3 in. ×3 in square. At each point on the grid the 256 backscattered waveforms were digitized into eight-bit, 512 word records that were averaged and then stored on computer for off-line analysis.

## ANALYSIS

### Entropy Analysis of Waveforms

All RF data are obtained by sampling a continuous function, $y = f(t)$, which is the backscattered waveform. We employ the convention that the domain of $f(t)$ is $[0, 1]$.

For $f(t)$, the signal energy is

$$E_f = \int_0^1 f(t)^2 dt \tag{1}$$

We may also compute a limiting form of Renyi's entropy given by

$$I_{f,\infty} = \log\left[\sum_{\{t_k|f'(t_k)=0\}} \frac{1}{|f''(t_k)|}\right], \tag{2}$$

which has demonstrated sensitivity to subtle changes in scattering architecture in several ultrasonic studies[3, 18].

The joint entropy of backscattered radio frequency waveforms, $f(t)$, and a reference function, $g(t)$, in the case where $f(t), g(t)$ are differentiable functions is[4]

$$H_{f,g} \equiv -\frac{1}{2}\int_0^1 dt\ \frac{\min[|f'(t)|, |g'(t)|]}{\max[|f'(t)|, |g'(t)|]} - \int_0^1 dt\ \log\left[\max[|f'(t)|, |g'(t)|]\right]. \tag{3}$$

A good choice for the reference waveform, $g(t)$, is frequently the reflection from a stainless steal plate of the emitted pulse from the insonifying transducer[4]. However, it is possible to significantly improve upon this.

## Optimal References for Joint Entropy Analysis

Previous comparisons of the sensitivity entropy and energy imaging have been based on the noise-normalized change in receiver value (also defined as the confidence[19]).[18, 4] For $n$ experimental measurements of the change $\Delta_i$, it is given by

$$c \equiv \frac{\text{mean}(\{\Delta_i : i = 1, \ldots, n\})}{\text{standard error}(\{\Delta_i : i = 1, \ldots, n\})}. \tag{4}$$

It is essentially a noise-normalized measure of change in an experimentally measured quantity.

For evaluation of receiver sensitivities in theoretical studies, we could maximize the similar quantity

$$\frac{\left\langle \delta H_{f,g} \right\rangle}{\sqrt{\text{Var}\left[\delta H_{f,g}\right]}}, \frac{\left\langle \delta E_f \right\rangle}{\sqrt{\text{Var}\left[\delta E_f\right]}}. \tag{5}$$

These relations may be derived by assuming that the experimental sources of noise are Gaussian. It is also necessary to model the measurement of each digitized point in the waveform as a convolution of the backscattered wave with a unit height square digitizer of extremely narrow width, $\Delta$. These assumptions lead to general criteria for an optimum reference, $g(t)$, which may be used to detect slight changes in backscattered waveform $f(t)$ using $H_{f,g}$.

Using these, we find that the average, or expected value, of the variation, $\langle \delta H_{f,g} \rangle$ can then be made larger than the expected variation of the signal energy $\langle \delta E_f \rangle$.

On the other hand, if $|g'(t)| \gg \Delta$, then the variances also obey the inequality: $\text{Var}\left[\delta H_{f,g}\right] \sim M_1\Delta < M_2\sqrt{\Delta} \sim \text{Var}\left[\delta E_f\right]$, where $M_1, M_2$ are constants independent of $\Delta$.

Thus, for appropriately chosen references, $g(t)$, the noise-normalized variations, which we take as a measure of sensitivity obey

$$\frac{\langle \delta H_{f,g} \rangle}{\sqrt{\text{Var}\left[\delta H_{f,g}\right]}} < \frac{\langle \delta E_f \rangle}{\sqrt{\text{Var}\left[\delta E_f\right]}}. \tag{6}$$

There are many such $g(t)$. Roughly, a good way to construct examples is to pick a zero, $t_0$, of $f_r'(t)$ and have $g'(t)$ be a large constant on one side of $t_0$, while on the other side it differs from $f_r'(t)$ by only a small constant $1 \gg \omega > 0$.

For instance, choosing $\omega = \Delta^{1/4}$ and setting $g'(t) = f_f'(t) - \omega$ for $t < t_0$ and $g'(t) = \gamma \gg 1$ for $t > t_0$, results in a joint entropy sensitivity of $O[\Delta^{-1/2}\log[\Delta]]$. On the other hand the signal energy will have confidence $O[\Delta^{-1/4}]$. The exact details for these calculations have been published elsewhere.[17]

In practice, the exact waveform and its variation are rarely known with any precision. This is especially true in a situation such as the current study where the variation almost certainly changes with location of the transducer during data acquisition. However, it still might be possible to find a single reference is nearly optimum at all locations using the calculations referred to above as general guidelines. These suggest that a reference be chosen such that $g'(t)$ be comprised of step-like functions with a large magnitude alternating with a small, but definitely non-zero, value.

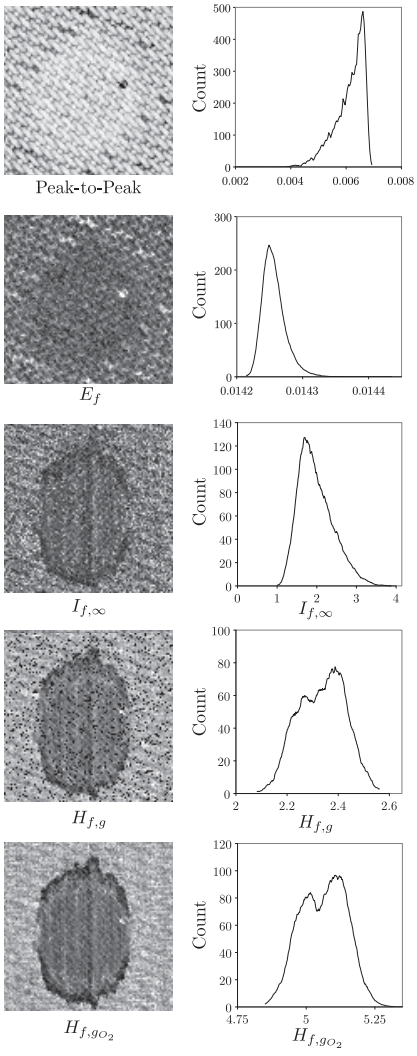


**FIGURE 2.** A comparison of different types of defect images all prepared from the same raw data. The entropy images all capture the true shape of the defect as verified by destructive examination of the specimen.

Functions of this form are essentially represented by specifying maximum and minimum heights and the locations of the jumps. Once these are chosen, a search over the parameter space may be conducted to find the best reference. We have found that a good starting point for this search is the reflection from the stainless steel-reflector. The waveform extrema of the waveform are chosen as the high to low transition points. The search then proceeds by shifting the waveform (for this study the shift values were: -0.02 to 0.10 in increments of 0.01) and/or dilations (with dilation factors ranging from 1.1 to 1.5 in 0.001 increments to the dilation factor). The high (ranging from 100.0 to 10000.0 in decades) and low(0.01 to 0.001 in decades) values were also varied. The search was first conducted using larger values for the enumerated increments, and the images assessed by computing the contrast between defect and defect regions as described below. Subsequently, the increments were decreased and the search refined to converge on an image having the highest quality.

## Projection-based Data Reduction

Optimal smoothing splines were fit to all waveforms as described elsewhere[18]. Subsequently, a "moving-window" analysis was performed using 128-point window that was shifted by 4 point steps along the waveform. The waveform segments within the moving window were used as $f(t)$ in either Eq. (1), (2), or (3) to produce energy or

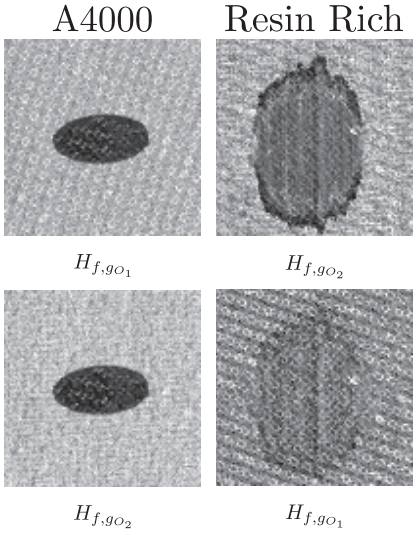


**FIGURE 3.** A comparison of images of different foreign objects made using different reference waveforms. Top row: images prepared using the respective "optimal" references found as described in the text. Bottom row: images prepared with the optimal references switched.

entropy images corresponding to successively deeper planes. Thus, the relatively large three dimensional raw data set was reduced to a subset of images (512 *vs*. 255) that record either the energy or information returning to the transducer as a function of depth. If the data set is small (*i.e.*, only a few dozen planes) and the defect is oriented in a volume that is relatively narrow and parallel to the planes, then it is frequently feasible to inspect each image plane as was done previously[4]. However, these are very specialized conditions.

A more robust approach would be to project the image planes by some mathematical operation onto a single plane in a manner that produces an image having high contrast and sharp border delineation between defect and defect-free regions of the specimen volume. This is roughly equivalent to rendering the non-defect regions of the specimen as semi-transparent medium in which the defects are suspended.

We have experimented with several mathematical operations for this purpose and found that for $E_f$ (and $\log[E_f]$), $I_{f,\infty}$ and $H_{f,g}$ images taking the minimum along the projection line produces images that most clearly display the defect and its boundary[17].

## Results and Discussion

A comparison of energy and entropy images is shown in Fig. (2). The histogram of pixel values is shown to the right of each image. The top row shows the result of peak-to-peak analysis of the backscattered waveforms. While this type of analysis is not the result of projecting different imaging planes, as are all other images in the figure, it is included due to the prevalence of this type of analysis in non-destructive testing. In the second row is the energy image obtained using Eq. (1). While there is some evidence of a defect in the center of the image, defect-to-background contrast is very poor, and there is no clear boundary between interior and exterior of the defect. In practice, moreover, this region would actually be part of a structure the size of a commercial aircraft wing, rendering its detection using energy imaging, unlikely. The poor defect-to-background contrast is consistent with the relatively narrow distribution of pixel values shown to the right of the image. The third row shows the $I_{f,\infty}$ obtained using Eq. (2) to analyze the waveforms. The defect-to-defect-free region contrast is visibly increased and there is a clearly defined boundary between the two regions. However, the pixel value histogram is still unimodal. It is intuitively obvious that an image having a bimodal distribution would have much better defect-to-defect-free region contrast. This is consistent with the image in the fourth row and its associated pixel value histogram. While not strictly bimodal the histogram is much wider than those of the preceding images. In the fifth row we see the image produced using the optimal reference, $g_{O_2}(t)$, which was identified after the type of computer search described above. The image has the highest defect-to-defect-free region contrast and its pixel value histogram is clearly bimodal. The lower peak corresponds to the pixels

within the defect boundary. We have also repeated, on the image in the fifth row, the contrast ratio analysis described in an earlier study.[9] The contrast ratio is -3.8 *vs.* at best 1.5 reported in the bottom row of Figure 6 contained in the earlier report. Thus, in addition to being better understood, the joint entropy analysis provides improved contrast to that obtained using the thermodynamic analysis.

In addition to the resin-rich specimen we have previously studied other types of foreign object inclusions in graphite/epoxy composites.[9]. One of these, designated as the A4000 specimen has also been subjected to the same type of optimization search as was the resin-rich specimen. In the top row of Fig. (3) we compare the "optimum" joint entropy for the A4000 specimen with the "optimum" joint entropy for the resin rich specimen (this panel also appeared in the bottom row of Fig. (2)). The defect-to-defect-free region contrast for the A4000 specimen is much higher than that of the resin-rich specimen which is consistent with observations of previous studies which demonstrated[9] that the A4000 inclusion was the easiest to detect. The histogram (not shown) of the pixel values in this image shows two widely separated peaks. Intuition would lead us to expect that the optimum reference is determined by the physical properties of the specimens and that each would have different optimum. This is indeed the case as indicated in the labels for the images in the top row of the figure ($H_{f,g_{o_1}}$ *vs.* $H_{f,g_{o_2}}$). This hypothesis is further tested in the second row, where we display the results of joint entropy analysis of the waveforms collected from each specimen using the optimum for the other specimen. The A4000 defect is so easy to image that the degradation of the defect-to-defect-free region contrast is hardly noticeable. However, for the resin-rich specimen there is clear deterioration.

## ACKNOWLEDGMENTS

This study was funded by NIH EB002168, 5R21EB018095, NSF DMS 1300280 and the PNNL Signature Discovery Initiative. The research was carried out at the Washington University Department of Mathematics and the School of Medicine.

## REFERENCES

1. M. Hughes, J. Marsh, A. Woodson, E. Lacey, C. Carradine, G. M. Lanza, and S. A. Wickline, Proceedings of the 2005 I.E.E.E. Ultrasonics Symposium 373 – 376 (2005).
2. M. S. Hughes, J. E. McCarthy, J. N. Marsh, J. M. Arbeit, R. G. Neumann, R. W. Fuhrhop, K. D. Wallace, T. Thomas, J. Smith, K. Agyem, D. R. Znidersic, B. N. Maurizi, S. L. Baldwin, G. M. Lanza, and S. A. Wickline, J. Acoust. Soc. Am. **125**, 3141–3145 (2009).
3. M. S. Hughes, J. E. McCarthy, M. Wickerhauser, J. N. Marsh, J. M. Arbeit, R. W. Fuhrhop, K. D. Wallace, T. Thomas, J. Smith, K. Agyem, G. M. Lanza, and S. A. Wickline, J. Acoust. Soc. Am. **126**, 2350–2358 (2009).
4. M. Hughes, J. McCarthy, J. Marsh, and S. Wickline, J. Acoust. Soc. Am. **133**, 283–300 (2013).
5. M. Hughes, Proceedings of the 1992 I.E.E.E. Ultrasonics Symposium **2**, 1205–1209 (1992).
6. M. Hughes, J. Acoust. Soc. Am. **93**, 892–906 (1993).
7. M. Hughes, Proceedings of the 1993 I.E.E.E. Ultrasonics Symposium **2**, 697–700 (1993).
8. M. Hughes, J. Acoust. Soc. Am. **95**, 2582–2588 (1994).
9. M. S. Hughes, J. N. Marsh, C. S. Hall, D. Savy, M. J. Scott, J. S. Allen, E. K. Lacy, C. Carradine, G. M. Lanza, and S. A. Wickline, I.E.E.E Transactions on Ultrasonics, Ferroelectrics, and Frequency Control **52**, 1555 – 1564 (2005).
10. M. S. Hughes, J. E. McCarthy, J. N. Marsh, J. M. Arbeit, R. G. Neumann, R. W. Fuhrhop, K. D. Wallace, D. R. Znidersic, B. N. Maurizi, S. L. Baldwin, G. M. Lanza, and S. A. Wickline, J. Acoust. Soc. Am. **121**, 3542–3557 (2007).
11. M. Hughes, G. M. Marsh, Lanza, S. A. Wickline, J. McCarthy, B. Wickerhauser, V. annd Maurizi, and W. K., J. Acoust. Soc. Am. **129**, 3756–67 (2011).
12. J. N. Marsh, J. E. McCarthy, M. Wickerhauser, J. M. Arbeit, R. W. Fuhrhop, K. D. Wallace, G. M. Lanza, S. A. Wickline, and M. S. Hughes, I.E.E.E. Transactions on Ultrasonics, Ferroelectrics and Frequency Control **57**, 1890–5 (2010).
13. J. N. Marsh, K. D. Wallace, G. M. Lanza, S. A. Wickline, M. S. Hughes, and J. E. McCarthy, 2010 I.E.E.E. Ultrasonics Symposium **1**, 53–56 (2010).
14. K. D. Wallace, J. Marsh, S. L. Baldwin, A. M. Connolly, K. Richard, G. M. Lanza, S. A. Wickline, and M. S. Hughes, I.E.E.E. Transactions on Ultrasonics Ferroelectrics and FrequencyControl **54**, 2291–2299 (2007).

15. M. Hughes, J. Marsh, K. Wallace, T. Donahue, A. Connolly, G. M. Lanza, and S. A. Wickline, Ultrasound in Medicine and Biology **33**, 1236–1243 (2007).
16. R. Seip, E. Ebbini, and M. O'Donnell, Proceedings of the 2005 I.E.E.E. Ultrasonics Symposium **2**, 1229–32 (1993).
17. M. Hughes, J. McCarthy, J. Marsh, and S. Wickline, Entropy **17**, 3518–3551 (2015).
18. M. Hughes, J. Marsh, K. Agyem, J. McCarthy, B. Maurizi, M. Wickerhauser, W. K.D., G. Lanza, and S. Wickline, IEEE Trans Ultrasonics Ferroelectrics and Frequency Control **58**, 2361–9 (2011).
19. D. L. Sackett, Can Med Assoc J **165**, 1226–1237Oct (2001).